

The Influence of Taylor Bubble Length on the Similarity of the Liquid Re-Circulation in Turbulent Flow Behind Solid and Gas Bubbles

Boonchai Lertnuwat

Dept. of Mechanical Engineering, Faculty of Engineering,
Chulalongkorn University, Phayathai Rd., Pathum Wan, Bangkok 10330, Thailand

Abstract

The similarity between flows induced by a solid Taylor bubble and a gas Taylor bubble is examined numerically using a Finite Volume Method. Although the similarity exists, it happens conditionally. In this work, it is found that the length of bubble plays an important role on the similarity. Short solid bubbles and gas bubbles tend to induce the same flow pattern behind themselves, whereas long bubbles tend to induce different flow structure behind themselves. This can be explained by the fact that long solid Taylor bubbles have more block ratio, leading to a serious velocity gradient at the cross section where a falling film jet detaches from the bubble. High wall shear stress is produced afterward, and it eventually affects the position of flow separation, which directly controls the geometry of toroidal vortex behind the bubble. Since there is no wall shear stress on a gas bubble surface, the geometry of toroidal vortex behind the solid bubble is different from that of the gas bubble if the wall shear stress is sufficiently high.

Keywords: Slug flow, Taylor bubble, Interfacial boundary condition, and Toroidal vortex

1. Nomenclature

D	Diameter of pipe	u_s	Tangential velocity
F_{Bs}	Body force in tangential direction	Y	The height of controlled volume covering boundary layer thickness
F_{Ss}	Surface forces in tangential direction	z	Coordinate on z-axis
L	The length of Taylor bubble	z_0	The position of bubble nose on z-axis
\dot{m}	The mass flow at the center of controlled volume	z_c	The position of vortex eye on z axis (mm)
$mf_{s,12}$	Momentum flux across side 1-2 in tangential direction	z_e	The position where the end of re-circulation occurs on z-axis (mm)
n	Normal axis over bubble surface	Δ	Total discrepancy of z_c , r_c and z_e between gas and solid bubble (mm)
$norm$	The relative norm of discrepancy between 2 bubbles, calculated by eq.(3)	δ	Boundary layer thickness
P	Pressure at the center of controlled volume	λ	The radius of $1/4$ circular curve, connecting bubble's side curve and bottom curve
R	The revolution radius of bubble surface about z-axis	θ	Relative angle relating local normal-tangential coordinates to the global cylindrical coordinates
r	Coordinate on r-axis	τ_w	Wall shear stress
r_c	The position of vortex eye on r-axis (mm)	τ_Y	Shear stress on surface Y
s	Distance along bubble surface	ρ	The density of liquid flowing over bubble surface
u_t	Terminal velocity of Taylor bubble		

2. Introduction

In engineering applications, pipelines often contain gas-liquid mixtures, which occur in many sorts of flows, e.g. bubble flow, slug flow, churn flow, annular flow and dispersed flow, depending on the gas-to-liquid ratio of the mixture. Among various flows, slug flow is an interesting kind of flow observed when a liquid is sucked from a deep well. Typically, slug flow is characterized by a succession of liquid slug separated by elongation bubbles (as shown in Fig.1a). Although, there may be many elongation bubbles in slug flow, slug flow is usually studied by dividing the flow into a unit for the sake of simplicity as seen in Fig.1(b). One unit of slug flow consists of liquid slug, falling film and one elongation bubble (so-called Taylor bubble). One of the interesting research topics in slug flow is to define the pressure drop across one slug unit, which mostly occurs in the region of the liquid slug [1, 2]. Since the pressure drop is the result of wall shear stress induced by the flow pattern behind the Taylor bubble, there are many researchers dedicated to the flow field behind a Taylor bubble. Hout *et al.* [3] studied the flow field around a Taylor bubble and found that the average flow field is confined within 12 times of the pipe-diameter ($12 D$) behind the bubble, whereas fluctuation lasts longer than which $50 D$, which results from the oscillation of the Taylor bubble. Bugg and Saad [4] reported that the average flow field terminates by $0.77 D$ behind the Taylor bubble and the rounded bottom of the Taylor bubble tends to decelerate the flow behind the bubble. The works stated above consider only the cases that a Taylor bubble rises along the centerline of a pipe, which is a general case of slug flow. However, a Taylor bubble sometimes sways from the pipe centerline, for instance, at the state of transition from slug flow to churn flow. Kawaji *et al.* [5] showed that a Taylor bubble rises up faster when it sways from the centerline of the pipe. In their experiment, a solid plastic bluff body was used instead of a gas bubble so that the position of the artificial bubble can be controlled. The artificial solid bubble was again exploited in [6] to confirm the reduction of drag on an eccentrically rising Taylor bubble. In that work, the effect of the deformed nose of the bubble was also investigated and it was found that the deformed nose reduces the drag force on a solid bubble. The use of a solid bubble is very

useful, but there is a suspicion whether a solid bubble induces the same flow field behind itself as a gas bubble does. Sotiriadis and Thorpe [7] investigated both flow fields and found that the similarity of flow field behind both types of bubbles is valid, although the interface conditions are different in both cases (liquid/solid and liquid/gas).

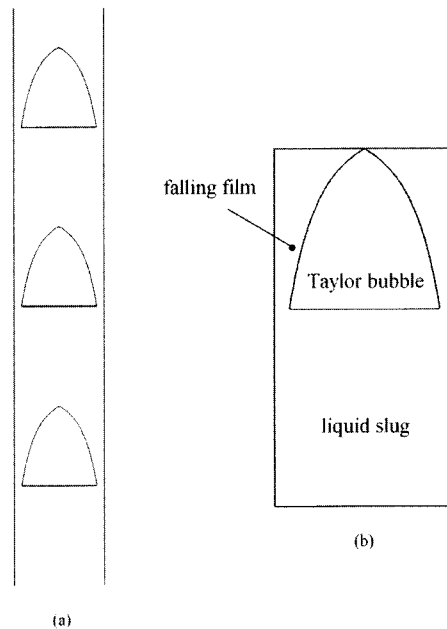


Fig.1: The schematic diagram of slug flow in the vertical pipe, (a) typical slug flow in the vertical pipe with series of Taylor bubbles, (b) the components in a slug unit.

Since in [7], the length of the solid bubble is selected to be 100 mm, the result is still not sufficient for concluding the existence of the similarity. The objective of this paper is to investigate the similarity between flow field induced by solid bubbles and gas bubbles at any length of a Taylor bubble by a numerical method.

3. Method: Numerical simulation

The flow field around a Taylor bubble is simulated using an implicit finite volume scheme with pressure-correction method. The simulation domain is bounded around a Taylor bubble as shown in Fig.2. The pipe diameter (D) is set to be 100 mm. According to [3] and [4], there is no velocity field in the region further

than 0.5 D in front of the bubble nose. Therefore, the computational domain starts at 2.75 D in front of the Taylor bubble to ensure the isolation of the bubble from the entrance effect. Behind the Taylor bubble, the computational domain is extended by 5.50 D.

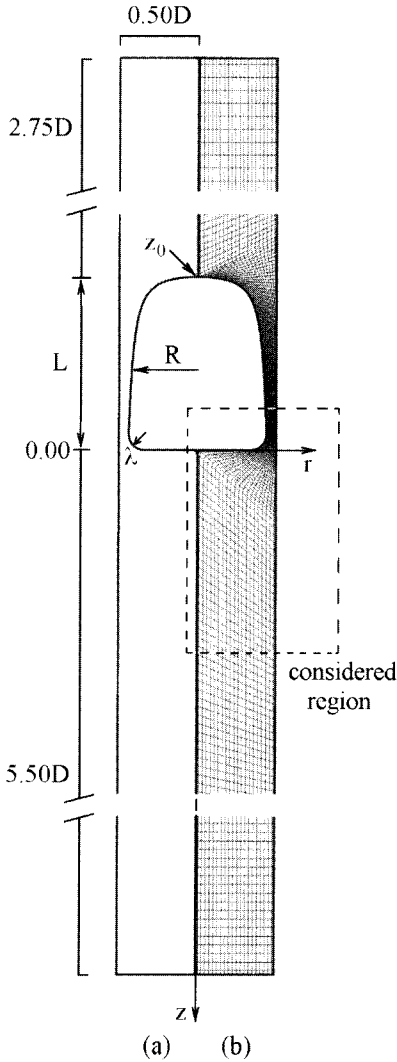


Fig.2: Computational domain, (a) the dimension of the computational domain and (b) the cylindrical-coordinates gridline-system used in this study and the considered region

Only the case that a Taylor bubble rises along the pipe centerline is considered, hence a

two-dimensional axisymmetry cylindrical coordinate system is employed, and only half of the pipe is simulated. The conventional $k-\epsilon$ model and wall function are selected as the simulation algorithm. The flow condition is statically steady state. The Taylor bubble rises in cylindrical pipe with terminal velocity calculated by the equation proposed by White *et al.* [8], which can be written as:

$$u_t = 0.345\sqrt{gD} \quad (1)$$

According to the objective of this work, 5 Taylor bubbles with different length, i.e. $L=25, 50, 100, 200$ and 400 mm, were simulated. To define the shape of bubble, the pressure drop in the falling film region is assumed to be zero as proposed in [1]. By exploiting Bernoulli's equation and eq.(1), we eventually obtain the equation for defining the shape of bubble as:

$$R = \frac{D}{2} \sqrt{1 - \sqrt{\frac{D}{D + 16.8(z - z_0)}}} \quad (2)$$

Besides, there is also a $\frac{1}{4}$ circular curve with radius of $\lambda=5$ mm, connecting the bubble's side curve and bottom curve as shown in Fig.2(a).

The interface boundary condition is different for the 2 types of bubbles. A no-slip condition is posed on the solid-bubble surface, resulting from the impermeable surface contacting the liquid. A free-shear condition is posed on the gas-bubble surface, due to the fact that gas density and viscosity inside the bubble is much lower than those of the liquid, leading to negligible shear force along the gas-bubble surface on the liquid side [1,9,10].

The pressure at the center of the upper boundary is set to be 100 kPa. While k and ϵ are set to be small values of $0.15 \times 10^{-3} \text{m}^2/\text{s}^2$ and $0.2 \times 10^{-3} \text{m}^2/\text{s}^3$, respectively, so that the conditions will be like single bubble flow in the pipe without disturbance in front of it. On the lower boundary, pressure is set to satisfy the conservation of mass, while the other variables are set to satisfy zero gradient. The boundary condition of a solid wall with zero velocity is posed on the right-hand-side boundary. For the left-hand-side boundary, the boundary condition in front of and behind the bubble is a symmetric plane, whereas the boundary condition on the

water-bubble interfacial surface is posed differently, depending on the type of bubble (i.e. solid or gas bubble) as explained above.

Since the structure of flow behind bubbles is considered, the following results will not be shown on the entire computational domain but only in the interesting region, defining as the considered region, shown in Fig.2(b).

4. Results

Fig. 3-7 show vector plots of the flow fields behind bubbles with different length (L), namely $L=25, 50, 100, 200$ and 400 mm, respectively. In each figure, two simulation results are shown. On the left hand side, flow induced by a gas bubble is illustrated, whereas flow induced by a solid bubble is shown on the right hand side.

The similarity between flow structure behind a solid bubble and a gas bubble is observed in Fig.3-5 (short bubble cases), but no longer found in Fig.6 and 7 (long bubble cases). The flow structures behind the bubbles in Fig.3-5 have quite the same pattern. To be specific, an annual jet from the end of the falling film region keeps attaching to the pipe wall. Although the jet expands along the main flow direction, the expansion rate is slow and cannot fulfill the region just behind the bubble bottom. This results in a cavity behind the bubble bottom where the toroidal vortex happens. This is almost the same in the case of long "solid" bubbles in Fig.6 and 7, but not for the case of long "gas" bubbles in Fig.6 and 7, where the annual jet no longer keeps attaching to the pipe wall. In contrast, the annual jet turns along the circular curve, resulting in two vortices; one behind the gas bubble and the other close to the pipe wall.

The simulation results shown in Fig.3-7 give only the qualitative comparison of the similarity. To obtain the quantitative comparison, some variables are to be taken for comparison. According to the past research [7], the similarity of flow structure behind the two bubbles is justified by the resemblance of the toroidal vortex behind these two bubbles, i.e. the position of the vortex eye and the end of the recirculation region (the stagnation point on the centerline of the pipe). Table 1 presents the geometry of toroidal vortexes induced by different bubbles.

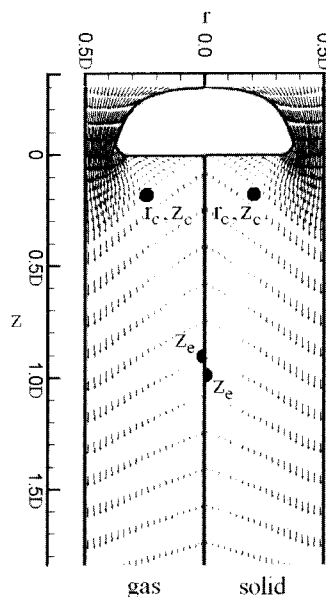


Fig.3: Comparison of flow induced by gas bubble (left) and solid bubble (right) of length (L) = 25mm.

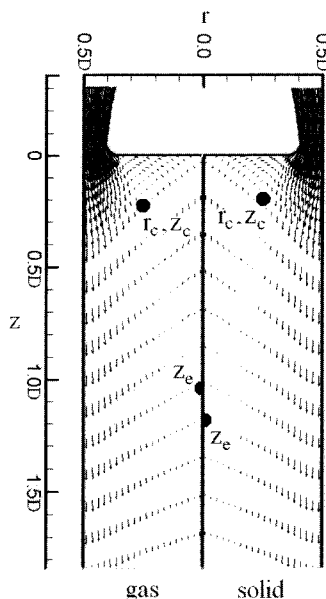


Fig.4: Comparison of flow induced by gas bubble (left) and solid bubble (right) of length (L) = 50mm.

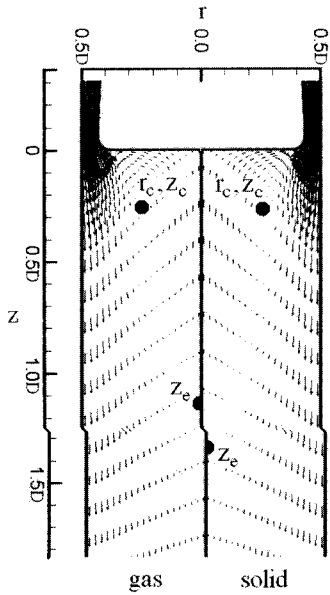


Fig.5: Comparison of flow induced by gas bubble (left) and solid bubble (right) of length (L) = 100mm.

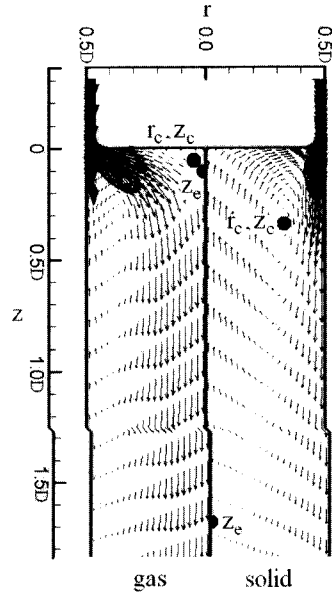


Fig.7: Comparison of flow induced by gas bubble (left) and solid bubble (right) of length (L) = 400mm

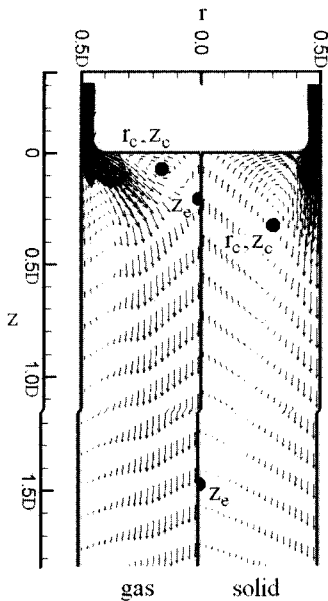


Fig.6: Comparison of flow induced by gas bubble (left) and solid bubble (right) of length (L) = 200mm.

Consistent with Fig.3-7, Table 1 shows that the difference between vortices generated by a gas bubble and a solid bubble is noticeable when L changes from 100 mm to 200 mm. This can be confirmed by a sudden increase of Δ . Relative comparison can be considered by relative *norm*, which also has a sudden increase after L is greater than 100 mm. (note that *norm* is calculated by eq.(3) and limited at $\sqrt{3}$).

Table 1: The geometry of toroidal vortices induced by a gas bubble and a solid bubble with different bubble lengths.

L		25	50	100	200	400
gas bubble	z_c	0.19	0.21	0.25	0.07	0.05
	r_c	0.23	0.26	0.26	0.18	0.08
	z_e	0.90	1.05	1.15	0.20	0.10
solid bubble	z_c	0.17	0.19	0.25	0.32	0.35
	r_c	0.20	0.24	0.28	0.30	0.33
	z_e	1.00	1.20	1.35	1.47	1.69
Δ		0.11	0.15	0.20	1.30	1.64
<i>norm</i>		0.22	0.18	0.16	1.23	1.48

$$norm = \left\{ \left[\frac{(z_{c,gas} - z_{c,solid})^2}{z_{c,solid}^2} \right] + \left[\frac{(r_{c,gas} - r_{c,solid})^2}{r_{c,solid}^2} \right] + \left[\frac{(z_{e,gas} - z_{e,solid})^2}{z_{e,solid}^2} \right] \right\}^{0.5} \quad (3)$$

5. Discussion

The previous section clearly shows that the similarity between toroidal vortexes induced by different bubbles exists with some conditions. That is, long bubbles cannot maintain the similarity. Focusing on the region where the annual jet ejects from the falling film region to the region behind the bubble, an interesting phenomenon is observed.

Fig.8-12 show the separation point on the solid bubble surface. It is obscurely evident that the position of the separation point occurs on the bubble bottom in the case of short bubbles ($L \leq 100$ mm: Fig.8-10) but occurs on the circular curve in the case of long bubbles ($L > 100$ mm: Fig.11&12). This observation can be used as an indicator for predicting the existing of similarity. In other words, the similarity between vortexes induced by different bubbles happens when the separation point occurs only on the bubble bottom.

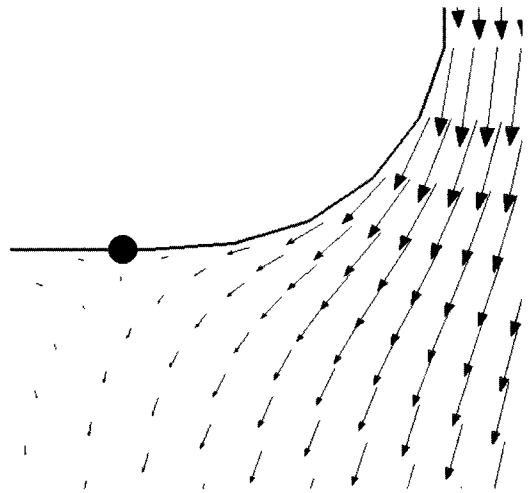


Fig.9: Separation point (dot) occurring on the solid bubble surface in the case that bubble length (L) is 50mm.

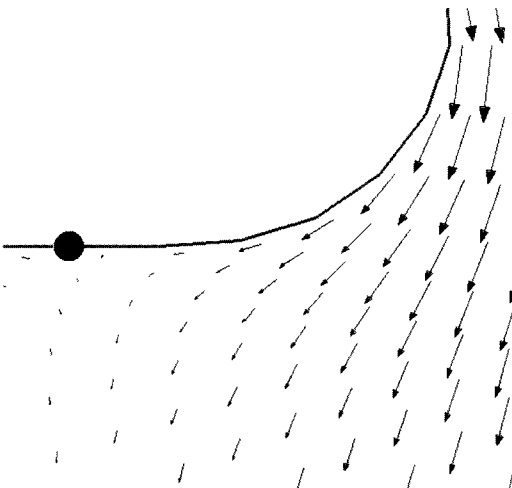


Fig.8: Separation point (dot) occurring on the solid bubble surface in the case that bubble length (L) is 25mm.

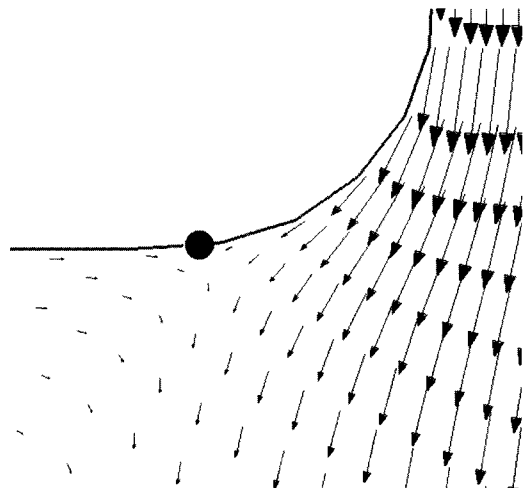


Fig.10: Separation point (dot) occurring on the solid bubble surface in the case that bubble length (L) is 100mm.

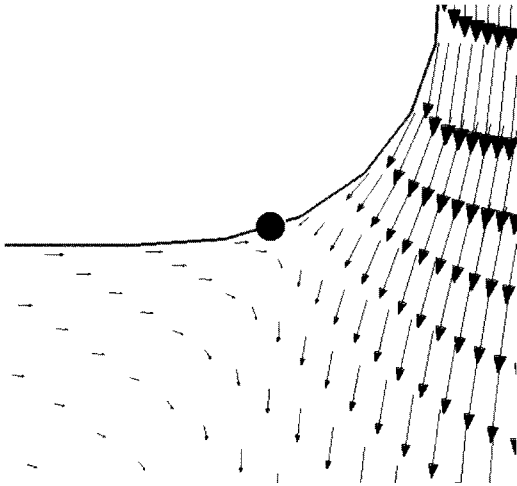


Fig.11: Separation point (dot) occurring on the solid bubble surface in the case that bubble length (L) is 200mm.

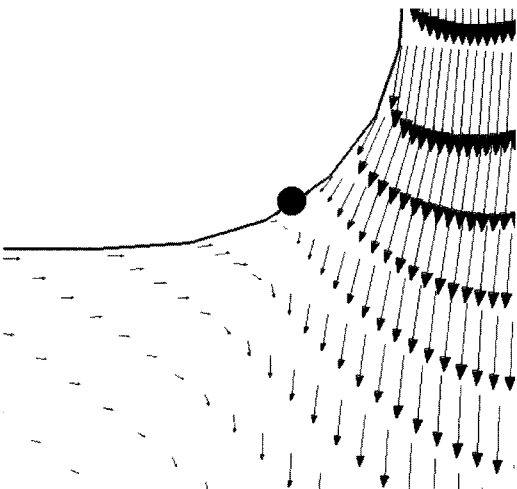


Fig.12: Separation point (dot) occurring on the solid bubble surface in the case that bubble length (L) is 400mm.

To explain the reason why the separation point occurs on the circular curve close to the end of the falling film region in the case of long bubbles, the momentum equation along the bubble surface must be reviewed. Fig.13 shows the schematic diagram used to derive the momentum equation along a Taylor bubble surface. The local normal-tangential coordinates related to the global cylindrical coordinates with

angle θ is shown in Fig.13(a). Next, Fig.13(b) shows the dimension of the controlled volume used for the following derivation, in which n is the normal axis and s is the tangential axis of the certain controlled volume. Herein, Y is the height of the controlled volume, which is larger than the boundary layer thickness, but much less than the radius of revolution (R), i.e. $\delta < Y \ll R$. Finally, Fig.13(c) demonstrates the forces per area surrounding the controlled volume (a-b-c-d).

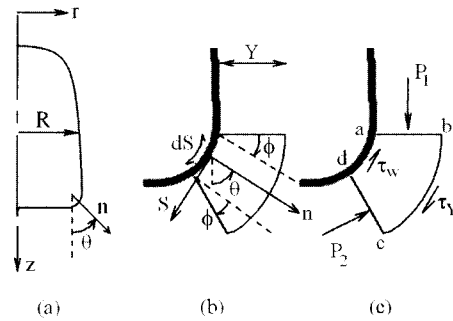


Fig.13: Schematic diagram for deriving the change of flow momentum along Taylor bubble surface, (a) the normal axis with respect to cylindrical coordinates, (b) dimension of the considered controlled volume and (c) forces per area surrounding the controlled volume.

Similar to the method proposed by Kays *et al.* [11], the continuity equation along the Taylor bubble surface is manipulated first to balance the mass flow penetrating around the controlled volume. Considering the controlled volume (a-b-c-d) in Fig.13(c), for steady flow, the balance of mass flow can be written as:

$$\dot{m}_{ab} + \dot{m}_{bc} + \dot{m}_{cd} + \dot{m}_{ad} = 0 \quad (4)$$

By using Taylor series, the mass flow across side a-b and c-d can be written as follows:

$$\begin{aligned} \dot{m}_{ab} &= - \left[\dot{m} - \frac{1}{2} \frac{\partial \dot{m}}{\partial s} ds \right] \\ &= - (2\pi R) \int_0^Y \rho u_s \cdot dn \end{aligned}$$

$$+ \frac{1}{2} \frac{\partial}{\partial s} \left[(2\pi R) \int_0^y \rho u_s \cdot dn \right] ds \quad (5)$$

$$\begin{aligned} \dot{m}_{cd} &= + \left[\dot{m} + \frac{1}{2} \frac{\partial \dot{m}}{\partial s} ds \right] \\ &= + (2\pi R) \int_0^y \rho u_s \cdot dn \\ &+ \frac{1}{2} \frac{\partial}{\partial s} \left[(2\pi R) \int_0^y \rho u_s \cdot dn \right] ds \quad (6) \end{aligned}$$

Since there is no blowing flow across side a-d, i.e. $\dot{m}_{ad} = 0$, substituting eq.(5) and eq.(6) into eq.(4), the mass flow across side b-c is obtained as:

$$\dot{m}_{bc} = - \frac{\partial}{\partial s} \left[(2\pi R) \int_0^y \rho u_s \cdot dn \right] ds \quad (7)$$

For steady state, the momentum equation of the controlled volume can be written as:

$$\begin{aligned} F_{Ss} + F_{Bs} \\ = mf_{s,ab} + mf_{s,cd} + mf_{s,bc} + mf_{s,ad} \quad (8) \end{aligned}$$

Each term in eq.(8) can be expressed individually as follows. Surface forces are composed of four components on each side of the controlled volume, shown in Fig.13(c), which can be written as:

$$F_{Ss,ab} = (2\pi R)Y \left(P - \frac{1}{2} \frac{\partial P}{\partial s} ds \right) \cos \phi \quad (9a)$$

$$F_{Ss,cd} = (2\pi R)Y \left(P + \frac{1}{2} \frac{\partial P}{\partial s} ds \right) \cos \phi \quad (9b)$$

$$F_{Ss,bc} = (2\pi R)\tau_y \cdot ds \quad (9c)$$

$$F_{Ss,ad} = (2\pi R)\tau_w \cdot ds \quad (9d)$$

Where $\phi = 0.5(\partial\theta/\partial s)ds$, which can be written in another form as $\phi = 0.5(1/\lambda)ds$. So the summation of surface forces yields:

$$F_{Ss} = F_{Ss,ab} + F_{Ss,cd} + F_{Ss,bc} + F_{Ss,ad}$$

$$F_{Ss} = -(2\pi R) \left[Y \frac{\partial P}{\partial s} ds \cdot \cos \phi + (\tau_w - \tau_y) ds \right]$$

τ_y is approximated to be zero, since the velocity gradient above the boundary layer thickness is very small. Hence, the approximate summation of surface forces is written as:

$$F_{Ss} = -(2\pi R) \left[Y \frac{\partial P}{\partial s} ds \cdot \cos \phi + \tau_w ds \right] \quad (10)$$

The body force in the tangential direction is expressed easily by projecting the gravity force of the controlled volume on z-axis, resulting in:

$$F_{Bs} = (2\pi R)Y\rho g \sin \theta \cdot ds \quad (11)$$

Then, the momentum fluxes on each side of the controlled volume are defined as:

$$\begin{aligned} mf_{s,ab} &= - \left\{ mf - \frac{1}{2} \frac{\partial}{\partial s} [mf] ds \right\} \cos \phi \\ &= - \left\{ (2\pi R) \int_0^y u_s \rho u_s \cdot dn \right. \\ &\quad \left. - \frac{1}{2} \frac{\partial}{\partial s} \left[(2\pi R) \int_0^y u_s \rho u_s \cdot dn \right] ds \right\} \cos \phi \quad (12a) \end{aligned}$$

$$\begin{aligned} mf_{s,cd} &= + \left\{ mf + \frac{1}{2} \frac{\partial}{\partial s} [mf] ds \right\} \cos \phi \\ &= + \left\{ (2\pi R) \int_0^y u_s \rho u_s \cdot dn \right. \\ &\quad \left. + \frac{1}{2} \frac{\partial}{\partial s} \left[(2\pi R) \int_0^y u_s \rho u_s \cdot dn \right] ds \right\} \cos \phi \quad (12b) \end{aligned}$$

$$\begin{aligned} mf_{s,bc} &= u_y \cdot \dot{m}_{bc} \\ &= -u_y \frac{\partial}{\partial s} \left[(2\pi R) \int_0^y \rho u_s \cdot dn \right] ds \quad (12c) \end{aligned}$$

$$mf_{s,ad} = 0 \quad (12d)$$

Finally, substitute eq.(10), eq.(11) and eq.(12a-d) into eq.(8), resulting in:

$$\begin{aligned}
 & (2\pi R) \left[-Y \frac{\partial P}{\partial s} \cos \phi - \tau_w + Y \rho g \sin \theta \right] ds \\
 & = \left\{ \frac{\partial}{\partial s} \left[(2\pi R) \int_0^y u_s \rho u_s \cdot dn \right] \cos \phi \right. \\
 & \quad \left. - u_y \frac{\partial}{\partial s} \left[(2\pi R) \int_0^y \rho u_s \cdot dn \right] \right\} ds \\
 \\
 & R \left[Y \rho g \sin \theta - Y \frac{\partial P}{\partial s} \cos \phi - \tau_w \right] \\
 & = \frac{\partial}{\partial s} \left[R \int_0^y u_s \rho u_s \cdot dn \right] \cos \phi \\
 & \quad - u_y \frac{\partial}{\partial s} \left[R \int_0^y \rho u_s \cdot dn \right] \\
 \\
 & \frac{1}{R} \frac{\partial}{\partial s} \left[R \int_0^y u_s \rho u_s \cdot dn \right] \cos \phi \\
 & = Y \rho g \sin \theta + \frac{u_y}{R} \frac{\partial}{\partial s} \left[R \int_0^y \rho u_s \cdot dn \right] \\
 & \quad - Y \frac{\partial P}{\partial s} \cos \phi - \tau_w \quad (13)
 \end{aligned}$$

On the left hand side of eq.(13), the rate of momentum change along the s-direction is explicitly shown, whereas the source terms are shown on the right hand side. The rate of momentum change along the s-direction implies the occurrence of separation. If the momentum of flow is decreased to a value, flow separation will take place. In accordance with eq.(13), the change of momentum flux depends on four parameters:

1. the projection of body force on the z-axis.
2. momentum flux leaving the controlled volume across side b-c.
3. pressure gradient across the controlled volume along the s-direction.
4. wall shear force.

The first term on the right hand side of eq.(13) (gravity force) always increases momentum flux. The magnitude of increasing

rate is dependent on the angle θ , which becomes zero along the bubble bottom curve. Hence, this term retards the occurrence of flow separation.

The fourth term on the right hand side of eq.(13) is only a different term between the solid and gas bubble cases. In the case of a solid bubble, this term is greater than zero. But this term is definitely zero in the case of a gas bubble, because of the free-shear condition posed on the bubble surface. In the case of a solid bubble, the presence of this term decreases the momentum flux. The greater the wall shear force is, the more rapid separation occurs. If the wall shear is sufficiently high, flow separation will happen on the circular curve, instead of the bubble bottom. Basically, wall shear is dependent on the velocity gradient, which becomes larger when the gap between the bubble surface and the pipe wall becomes narrower. By considering eq.(2), it is clear that a longer Taylor bubble (with larger z) has a larger R , leading to a narrower gap between the bubble surface and the pipe wall. The narrower gap produces a more serious velocity gradient. This promotes a greater wall shear, causing flow separation to occur rapidly. Finally, in the case of a long bubble, the separation point takes place on the circular curve connecting the bottom curve and the side curve of the Taylor bubble, as already shown in Fig.11 and 12.

Moreover, the second term and the third term on the right hand side of eq.(13) will show their influence when a separation point takes place on the circular curve. More momentum flux leaves the controlled volume across side b-c, since flow cannot turn along the circular curve. When mass flux leaves the controlled volume across side b-c, the value of the second term is negative. This causes a reduction of momentum flux. It, thus, accelerates flow separation to occur more rapidly.

The third term on the right-hand-side of eq.(13) refers to pressure gradient, which is often assumed to be equal to the gradient of momentum flux of flow above the boundary layer thickness, that is:

$$\frac{\partial P}{\partial s} = -\rho u_y \frac{\partial u_y}{\partial s} \quad (14)$$

Eq.(14) shows that pressure gradient is a negative function of velocity gradient, which

will be larger if mass flux cannot flow along the circular curve (presence of wake). This term, thus, reduces the momentum flux and accelerates the flow separation to happen as well.

In short, the process above can be explained as:

1. A Longer solid bubble has a larger block ratio, resulting in a more serious velocity gradient.

2. Once the velocity gradient is high enough to produce high wall shear stress on the solid bubble surface, flow separation will occur on the circular curve.

3. The separation point on the circular curve prevents mass flux to flow across side c-d of the controlled volume. More mass flux leaves the controlled volume across side b-c, resulting in flow separation happening more rapidly.

4. Pressure gradient also accelerates flow separation to occur since it relates to a negative velocity gradient of flow above the boundary layer thickness.

6. Conclusion

The $k-\varepsilon$ model is discretized with a finite volume method to investigate the effect of bubble length on the similarity of the flow structure induced behind a solid and a gas bubble. Five different bubble lengths were selected to be simulated. The results of simulation can be concluded as:

1. Similarity is limited by the length of the Taylor bubble since a longer bubble produces a higher velocity gradient, resulting in more shear stress on the solid bubble surface.

2. The position of the separation point on the bottom of Taylor bubble may be used as an indicator to predict the similarity, i.e. the similarity of flow field between a solid bubble and a gas bubble disappears when the separation point occurs on the circular curve of the solid bubble. This is useful for researchers because it helps them to make a decision for eliminating data referred to as similarity when the phenomenon happens.

3. Using a solid bubble to study the characteristic of flow structure behind a gas bubble is not always applicable, but limited to a certain bubble length. This leads to serious concerns for experiments. For example, if one wants to utilize a long solid bubble as a long gas bubble, one needs to reduce wall shear on the solid bubble by reducing turbulent viscosity.

7. References

- [1] Barnea, D., Effect of Bubble Shape on Pressure Drop Calculations in Vertical Slug Flow, *Int. J. Multiphase Flow*, Vol.16 No.1, pp.79-89, 1990.
- [2] Levy, S., *Two-phase flow in Complex Systems*, John Wiley & Sons, USA, pp. 192-215, 1999.
- [3] Hout, R.V., Gulitski, A., Barnea, D., and Shemer, L., Experimental investigation of the Velocity field Induced by a Taylor Bubble Rising in Stagnant Water, *Int. J. Multiphase Flow*, Vol.28, pp.579-596, 2002.
- [4] Bugg, J.D. and Saad, G.A., The Velocity Field Around a Taylor Bubble Rising in a Stagnant Viscous fluid: Numerical and Experimental Results, *Int. J. Multiphase Flow*, Vol.28, pp.791-803, 2002.
- [5] Kawaji, M., DeJesus, J.M., and Tudose G., Investigation of flow Structures in Vertical Slug flow, *Nuclear Engineering and Design*, Vol.175, pp.31-48, 1997.
- [6] Tudose, E. T. and Kawaji, M., Experimental Investigation of Taylor Bubble Acceleration Mechanism in Slug Flow, *Chemical Engineering Science*, Vol.54, pp.5761-5775, 1999.
- [7] Sotiriadis, A. A. and Thorpe, R. B., Liquid Re-Circulation in Turbulent Vertical Pipe Flow behind a Cylindrical Bluff Body and Ventilated Cavity Attached to a Sparger, *Chemical Engineering Science*, Vol.60, pp.981-994, 2005.
- [8] White, E. T., and Beardmore, R. H., The Velocity of Rise of Single Cylindrical Air Bubbles Through Liquids Contained in Vertical Tubes, *Chemical Engineering Science*, Vol.17, pp.351-361, 1962.
- [9] Clarke, A., and Issa, R. I., A Numerical Model of Slug Flow in Vertical Tubes, *Computers & Fluids*, Vol.26 No.4, pp.395-415, 1997.
- [10] Mao, Z.-S., and Dukler, A.E., The Motion of Taylor Bubbles in Vertical Tubes. I. A Numerical Simulation for the Shape and Rise Velocity of Taylor Bubbles in Stagnant and Flowing Liquid, *Journal of Computational Physics*, Vol.91, pp.132-160, 1990.
- [11] Kays, W. M., and Crawford, M. E., *Convective Heat and Mass Transfer*, 3rd ed., McGraw Hill pub., Singapore, pp.68, 1993.